Journal of Alloys and Compounds 504S (2010) S283–S287

Contents lists available at ScienceDirect

Journal of Alloys and Compounds

journal homepage: www.elsevier.com/locate/jallcom

Preparation and characterization of highly amorphous HVOF stainless steel coatings

D. Zois[a,b], A. Lekatou[a,*], M. Vardavoulias[b]

[a] Department of Materials Science and Engineering, University of Ioannina, 45111 Ioannina, Greece
[b] Pyrogenesis SA, Technological Park of Lavrion, 19500 Lavrion, Greece

ARTICLE INFO

Article history:
Received 2 July 2009
Received in revised form 16 January 2010
Accepted 10 February 2010
Available online 18 February 2010

Keywords:
Nanostructured steel
Coating materials
Thermal spraying
Corrosion
X-ray diffraction

ABSTRACT

A partially amorphous FeCrMoWBCSi powder has been HVOF sprayed in order to produce highly amorphous coatings. The extinction or retention of crystalline phases due to the spraying process is discussed. Amorphicity in coatings is associated with a high melting degree. The latter is attained by a high particle temperature and sufficient residence time in the flame. Coating properties, such as porosity, microhardness and adhesion strength are evaluated. The lowest coating porosity corresponds to the most amorphous coating. The least crystalline coating presents the highest corrosion resistance in 3.5% NaCl.

1. Introduction

A method of reducing the overall manufacturing costs of a Bulk Metallic Glass (BMG) component with superior properties is the deposition of metallic amorphous layers on metal substrates. The fabrication of amorphous coatings requires rapid quenching from the melt at cooling rates fast enough to suppress the nucleation and growth of competing crystalline phases [1]. One way to achieve this is to employ thermal spray processes. For example, Sampath [2] investigated the application of Air Plasma Spraying (APS) and Vacuum Plasma Spraying (VPS) to deposit Ni–Mo based metallic glass coatings (MGCs). The APS coatings contained defects such as porosity, insufficient interlamellar bonding, oxide inclusions, etc.; in the VPS coatings, crystalline structures had been developed, due to the absence of convective cooling.

It is conceivable that minimal oxide presence, minimal interconnected porosity and high amorphicity can significantly improve the corrosion performance of a coating. High Velocity Oxy-Fuel (HVOF) spraying may lead to lower oxidation than plasma spraying due to lower temperatures, and low coating porosity due to the supersonic velocities of the propelled particles [3]. However, complete amorphization during quenching might not be accomplished. For instance, HVOF NiCrMoB MGCs have been reported to consist of crystalline precipitates – Cr_2O_3, $NiCr_2O_4$ and M_3B_2 (M = Mo or Cr) – within an amorphous Ni-rich matrix [1].

Cost-wise, there is a growing interest in the employment of Fe and Cu-based BMGs, as potential replacements for the much more expensive Zr-, Ti-, Ni- and Ln-based alloys [4]. To date, the vast majority of the works on the corrosion behavior of Fe-based MGs refer to bulk materials [e.g. 5–9]. Regarding the corrosion behavior of high entropy coatings, an HVAF (High Velocity Air Fuel spraying) NiNbTiZrCoCu coating exhibited high corrosion resistance in aqueous HCl, though lower than that of the respective amorphous ribbons [10]. The corrosion resistance of an HVOF FeCrMoCBY coating in 1 M HCl was comparable to that of the bulk amorphous counterpart and superior to the corrosion resistance of electroplated Cr-based coatings [11]. Sputtered Fe–Ni–Cr–W MGCs presented excellent pitting resistance in neutral and acidic solutions, which was preserved after a crystallization heat treatment [12].

This work is part of a wider investigation on stainless steel high entropy coatings, aiming at identifying the HVOF spraying parameters under which the amorphous fraction is maximized and coating oxidation is minimized. The coatings are free of expensive rare earth metals, such as Y, Ga and lanthanides, which are usually added to amorphous steels as glass forming ability enhancers (GFA) [13,14].

2. Experimental

A gas atomized Fe–18.3Cr–7.7Mo–1.6W–1.8Mn–14.9B–3.6C–2.6Si powder (at.%) of nominal particle size (−53 + 10) μm, manufactured by the NanoSteel Co.,

* Corresponding author. Tel.: +30 26510 07309; fax: +30 26510 07034.
E-mail address: alekatou@cc.uoi.gr (A. Lekatou).

0925-8388/$ – see front matter © 2010 Elsevier B.V. All rights reserved.
doi:10.1016/j.jallcom.2010.02.062

Table 1
Spraying parameters.

Spraying series	Oxygen-to-fuel ratio	Total gas supply (l/min)	Spraying distance (mm)	Feed rate (g/min)	Power output (kW)	Particle temperature (°C)	Particle velocity (m/s)
NS_1	3.6	720	250	38	85	1583 ± 5	557 ± 29
NS_2	5.0	725	250	38	103	1723 ± 7	714 ± 19
NS_3	6.4	735	250	38	108	1658 ± 5	725 ± 26

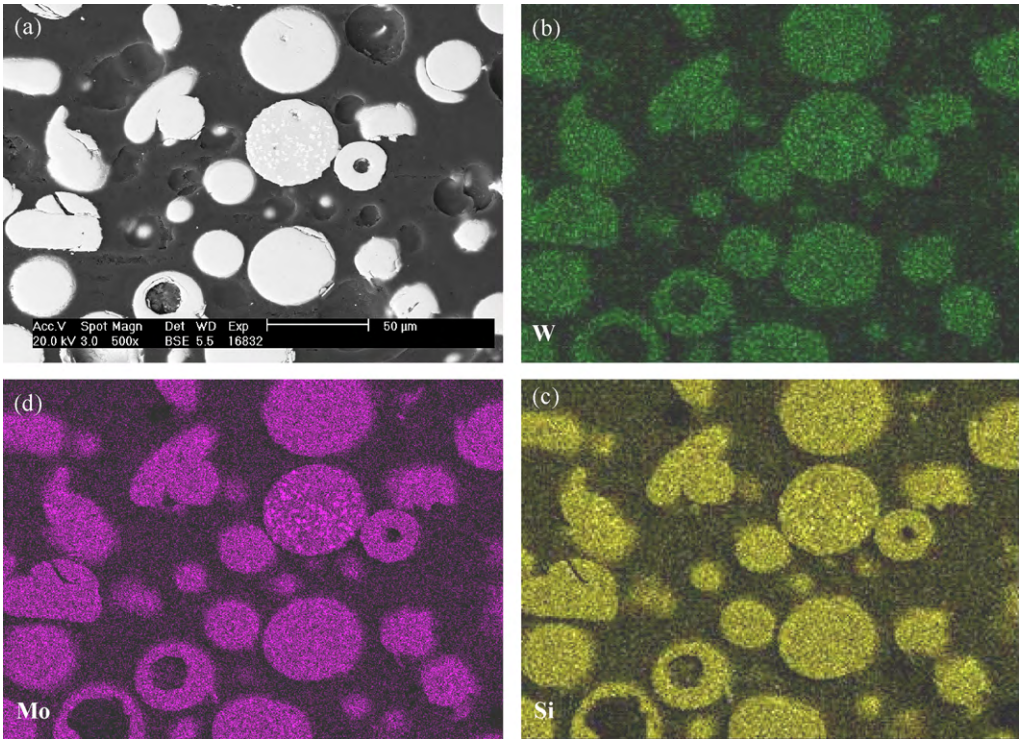

Fig. 1. Cross-section of the powder feedstock and elemental mapping.

was HVOF sprayed on 304 stainless steel coupons. Spraying was performed by a Sulzer Metco 2700 Hybrid torch. During spraying, particle temperatures and velocities were recorded by the Oseir Spraywatch 3i system. Three spraying series were conducted, where the principal variable was the oxygen-to-fuel (propane) ratio. The spraying parameters are given in Table 1.

The powder and the coatings were microstructurally characterized by SEM-EDX (Philips XL 40 SFEG). Microhardness was measured by a Shimadzu tester (14 measurements per coating). The coating adhesion strength (3 measurements per torch power) was measured by a portable elcometer (110 P.A.T.T.I.®) according to ASTM C633-01. XRD patterns were obtained by a Bruker D8 Advance diffractometer.

Potentiodynamic polarization tests were performed on coupons ground to 1000 grit and encapsulated in epoxy, so that a surface area of ~1 cm^2 was exposed to aerated 3.5% NaCl at ambient temperature (Gill AC potentiostat by ACM Instruments, scan rate: 10 mV/min). A standard three-electrode cell was employed, with Ag/AgCl as the reference electrode and a platinum gauge as the counter electrode. Corrosion current densities were determined by Tafel extrapolation [15].

3. Results and discussion

3.1. Feedstock characterization

Fig. 1a shows that the powder particles have a spherical shape due to the gas atomization processing. Some particles are hollow, a typical consequence of the atomization process. Precipitates rich in W, Mo and Si are often observed within the coarsest particles (Fig. 1b, c and d).

The XRD spectrum of the powder shows a hump typical of amorphicity (Fig. 2). Peaks corresponding to crystalline phases are also observed: martensite ($Fe_{1.86}C_{0.14}$); borides of stoichiometries similar to $Cr_{1.65}Fe_{0.35}B_{0.96}$, t-$Fe_3B$, $Fe_{23}B_6$; borocarbide of stoichiometry similar to $Fe_{23}(B,C)_6$. Mo and Cr may also be contained in the borides due to their high combining tendency with B [16]. In addition, Cr, Mo and Si (to a lesser extent) may form substitutional solid solutions with α-Fe in a wide range of compositions [17]; hence, the possibility of participating in all the detected phases is strong. The existence of borides could be harmful to the amorphous state,

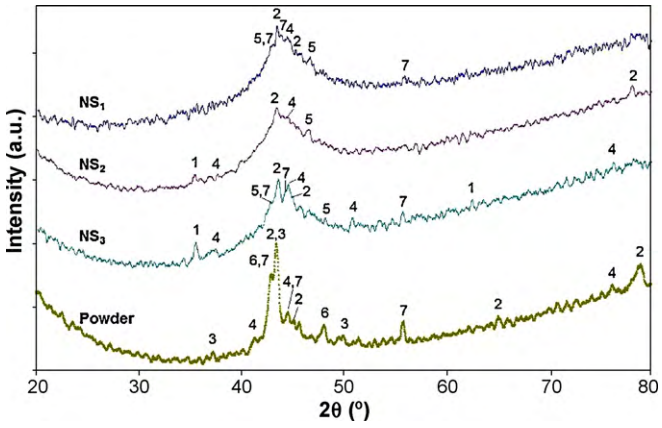

Fig. 2. XRD patterns of the powder and the coatings. 1: Fe_3O_4, 2: $Fe_{1.86}C_{0.14}$, 3: $Fe_{23}B_6$, 4: $Fe_{23}(B,C)_6$, 5: $Fe_{15}Si_3B_2$, 6: Fe_3B, 7: $Cr_{1.65}Fe_{0.35}B_{0.96}$. The above compositions are only indicative. The actual phases probably contain and other elements (Cr, Mo, Si, W) in solid solution with iron.

Table 2
Characteristic properties of the coatings.

Coating	Coating thickness (μm)	HV_{300}	Porosity (%)	Adhesion (MPa)
NS_1	150 ± 12	870 ± 52	1.0 ± 0.4	>60
NS_2	143 ± 20	826 ± 93	0.8 ± 0.3	>60
NS_3	157 ± 16	796 ± 93	1.1 ± 0.3	>60

because they lead to a reduced B content in the supercooled liquid, and, consequently, to a reduced GFA [18].

3.2. Spraying parameters

As shown in Table 1, the highest temperature is recorded at the intermediate oxygen-to-fuel ratio (NS_2); it would be expected that the highest temperature would be recorded at the highest ratio producing the highest power output (NS_3). It is postulated that ratios greater than 5 lead to reduced flame temperatures because of oxygen overload; on the other hand, ratios lower than 5 also lead to reduced flame temperatures, because of insufficient oxygen content. Critical oxygen-to-fuel ratios for maximum flame temperatures have also been noticed on spraying white cast iron [19] and NiTiZrSiZn amorphous coatings [20].

Table 1 shows that the particle velocities follow the order $NS_1 < NS_2 \cong NS_3$ in proportion to the power output.

3.3. Coating characterization

Table 2 shows low coating porosities. (It should be emphasized that the employed image analysis techniques can only identify the coarsest pores and give an overall view of the coating porosity.) NS_2 coating presents the lowest porosity due to the highest melting degree achieved at the highest particle temperatures. At high particle temperatures, molten material of high diffusivity fills the asperities and gaps of the previously deposited layers, leading to low porosities [21]. All the coatings present similar hardness values, which are substantially higher than the ones reported for stainless steel 304s [8] and stainless steel thermally sprayed coatings [3]. All the coatings present satisfactory adhesion strength.

Fig. 3 illustrates a cross-section of NS_1 coating. In all the coatings, a few coarse unmolten or semi-molten particles are discerned presenting dispersions of rectangular particles. EDX analysis revealed that these precipitates are (Mo,Cr,Fe,W) borocarbides or carbides. The main reasons for the presence of coarse unmelted particles in the coatings can be low particle temperatures (NS_1, Table 1) and/or

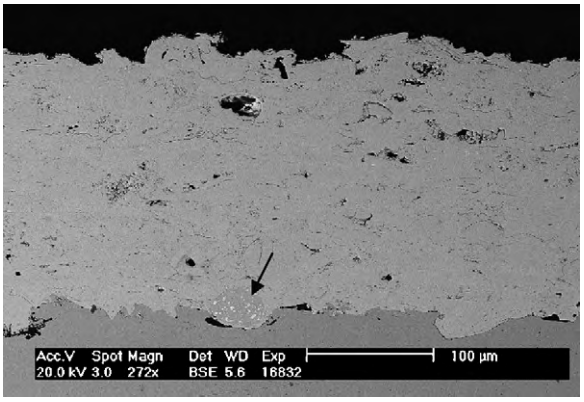

Fig. 3. Cross-section of NS_1 coating; the arrow points at a coarse unmelted particle with retained precipitates.

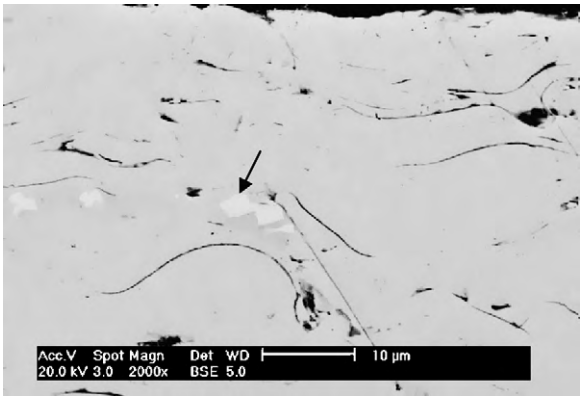

Fig. 4. Carbide particles (arrow pointed) along a splat layer (cross-section of NS_2 coating).

short residence time in flame caused by high particle velocities (NS_2, NS_3, Table 1). Isolated rectangular particles are also discerned in all the coatings. EDX analysis revealed that they are (Mo,Cr,Fe,W) borocarbides or carbides. All the coatings present inter-splat oxide stringers (dark contrast lines) running parallel to the substrate (Fig. 4).

Fig. 2 shows that the humps in the XRD spectra of the coatings are ampler than the humps in the powder spectrum. Also, the "crystalline" peaks of the coatings are notably weaker than those of the powder. The lower crystallinity of the coatings, as compared to the powder feedstock, can be explained by the quenching of fully molten particles to the glass state from their highest temperature, through the action of flattening onto the substrate surface [22].

Comparison of the XRD scans of the three coatings, shows that NS_2 coating exhibits minimal presence of 'crystalline' peaks, whilst its broad halo peak ($2\theta = 40–50^\circ$), is almost free of small 'crystalline' peaks. It seems that at the intermediate oxygen-to-fuel ratio, the temperature was high enough to melt most of the particles; at the same time, the particle velocity was high enough to ensure short particle residence in the flame and, consequently, low oxidation. NS_3 coating seems to present a higher crystalline fraction than NS_1 coating, despite the higher particle temperature. The higher crystalline fraction of NS_3, as compared to NS_1, is mostly indicated by the higher intensity peaks corresponding to $Cr_{1.65}Fe_{0.35}B_{0.96}$, $Fe_{23}(B,C)_6$ and Fe_3O_4, as well as the more distinct 'crystalline' peaks

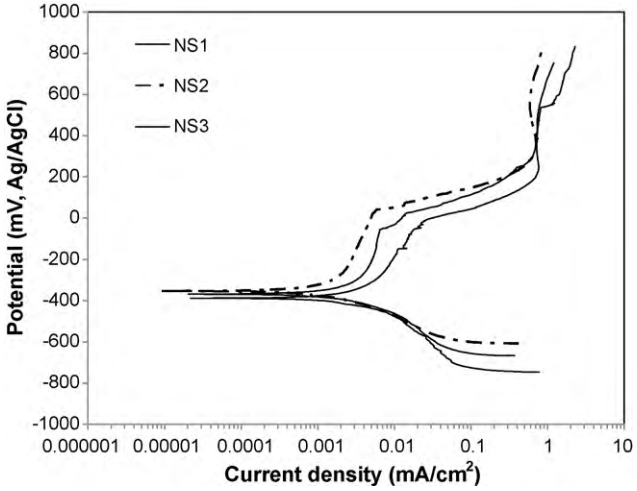

Fig. 5. Potentiodynamic polarization behavior of the coatings in 3.5% NaCl, at ambient temperature.

Table 3
Corrosion properties extracted from the voltammograms of Fig. 5 (E_{corr}: corrosion potential, i_{corr}: corrosion current density, i_p: current density at the first passive stage, E_b: breakdown potential after the first passive stage).

Coating	E_{corr} (mV vs. Ag/AgCl)	i_{corr} (mA/cm^2)	i_p (mA/cm^2)	E_b (mV vs. Ag/AgCl)
NS_1	−368	3.72×10^{-3}	0.004–0.007	−52
NS_2	−352	1.60×10^{-3}	0.002–0.006	41
NS_3	−387	4.74×10^{-3}	0.007–0.02	−18[a]

[a] Metastable pitting starts at −150 mV.

within the hump. The most oxidizing environment during spraying of NS_3 coating may account for its highest oxide content. The lower amorphicity of NS_3, as compared with NS_1, despite the higher particle temperature, is attributed to the higher particle velocity causing shorter particle residence in flame and, hence, less time for melting. A complementary reason for the relatively low amorphicity of NS_3 coating could be the insufficient GFA and/or cooling rate in regions of altered chemical compositions, such as the oxide stringer vicinity.

The precipitates of the type $Cr_{1.65}Fe_{0.35}B_{0.96}$, $Fe_{23}(B,C)_6$ (also detected in the pristine powder) have probably been retained in the coarsest powder particles, which were deposited semi-molten. Moreover, $Fe_{23}(B,C)_6$ is reported as a principal phase in the system Fe–B–C, at room temperature [23]. In the system Fe–B–X (X: any one or a combination of C and one or two of the most common of the first and second series transition elements), the main phases at room temperature are (Fe,X) and $(X,Fe)_2B$ – almost pure X_2B – [23]; this justifies the detection of $Cr_{1.65}Fe_{0.35}B_{0.96}$ in the coatings. The detection of $Fe_{15}Si_3B_2$ in the coatings is compatible with the suggestion that $Fe_3(Si,B)$ is a Si-stabilized phase originating from one of the metastable forms of Fe_3B [24].

M_3B and $M_{23}B_6$, which were present in the powder feedstock, are missing from the coatings or their peak intensity is notably reduced. The notable reduction or extinction of t-M_3B and fcc-$M_{23}B_6$ can be explained by their instability [16,25,26]. Upon spraying, the borides were dissolved in the Fe-melt. During quenching, the cooling rate was fast enough to suppress B segregation. The oversaturated Fe was cooled as martensite and/or glass.

The XRD results can justify the similar hardness values for the three coatings, given in Table 2. The hardness gained by the lower porosity [27] and the higher amorphicity of the NS_2 coating, as compared with NS_1 and NS_3, is offset by the hardness lost owing to the lower content of carbides, borides and oxides.

3.4. Corrosion behavior

The voltammograms of the deposited coatings in 3.5% NaCl, are illustrated in Fig. 5. The extracted corrosion values are given in Table 3. All the coatings exhibit passive behavior following the initial active state. (NS_3 coating does not really show a current stabilization trend, but rather a current limiting stage.) The subsequent sharp increase in current density at relatively low potentials, suggests breakdown of passivity by pitting. A second stage of current stabilization follows pitting; however, the high currents indicate the formation of highly unstable deposits in the pits.

The most amorphous coating (NS_2) presents the noblest corrosion potential, the lowest corrosion current density, the lowest passive current densities and the highest breakdown–pitting potential. The superior corrosion performance of NS_2 coating can be attributed to its higher amorphous fraction, in comparison with NS_1 and NS_3, since the homogeneous glass phase is expected to allow the growth of a uniform protective film. Furthermore, NS_2 coating presents the lowest possibility amongst the three coatings for galvanic effects between adjacent phases of different compositions and crystal structures. For instance, the presence of carbides in coatings reportedly accelerates microgalvanic corrosion [28]. A third reason for the corrosion resistance of NS_2 coating is its low porosity that reduces the chances for interconnected porosity. On the other hand, the lowest corrosion resistance is exhibited by the least amorphous and most porous coating, namely NS_3 coating.

4. Conclusions

The main conclusions drawn from the characterization of coatings manufactured by HVOF spraying of a FeCrMoWBCSi partially amorphous powder under three different oxygen-to-fuel ratios (3.6, 5 and 6.4), are:

1. The coatings present a higher amorphous fraction than the powder feedstock, owing to substantial melting during spraying and subsequent quenching to the glass state.
2. Spraying and quenching result in a significant decrease in the metastable boride phases.
3. Amorphicity in coatings is associated with a high melting degree. The latter is achieved by a high particle temperature (attained at a critical oxygen-to-fuel ratio: in this case around 5) and sufficient residence time in the flame (depending on the spraying particle velocity).
4. The highest oxidation levels correspond to the highest oxygen-to-fuel ratio.
5. The lowest coating porosity is attained at the highest temperature (i.e. intermediate oxygen-to-fuel ratio).
6. During potentiodynamic polarization in 3.5% NaCl, all the coatings show passivation disrupted by pitting.
7. A high amorphous fraction combined with low porosity benefits the corrosion resistance of a coating.

References

[1] A.H. Dent, A.J. Horlock, D.G. McCartney, S.J. Harris, Mater. Sci. Eng. A283 (2000) 242–250.
[2] S. Sampath, Mater. Sci. Eng. A167 (1993) 1–10.
[3] L. Pawloski, The Science and Engineering of Thermal Spray Coatings, Wiley, 1995.
[4] W.H. Wang, C. Dong, C.H. Shek, Mater. Sci. Eng. R 44 (2004) 45–89.
[5] H.X. Li, S. Yi, Mater. Chem. Phys. 112 (2008) 112–114.
[6] A. Lekatou, A. Marinou, P. Patsalas, M. Karakasides, J. Alloys Compd. 483 (2009) 514–518.
[7] J. Jayaraj, Y.C. Kim, K.B. Kim, H.K. Seok, E. Fleury, Sci. Technol. Adv. Mater. 6 (2005) 282–289.
[8] Y.Y. Chen, T. Duval, U.D. Hung, J.W. Yeh, H.C. Shih, Corros. Sci. 47 (2005) 2257–2279.
[9] M. Magrini, P. Matteazzi, A. Frignani, Mater. Chem. Phys. 13 (1985) 71–83.
[10] A.P. Wang, Z.M. Wang, J. Zhang, J.Q. Wang, J. Alloys Compd. 440 (2007) 225–228.
[11] H.S. Ni, X.H. Liu, X.C. Chang, W.L. Hou, W. Liu, J.Q. Wang, J. Alloys Compd. 467 (2009) 163–167.
[12] R. Wang, J. Non-Cryst. Solids 61&62 (1984) 613–618.
[13] Z.H. Gan, H.Y. Yi, J. Pu, J.F. Wang, J.Z. Xiao, Scripta Mater. 48 (2003) 1543–1547.
[14] Q.J. Chen, H.B. Fan, J. Shen, J.F. Sun, Z.P. Lu, J. Alloys Compd. 407 (2006) 125–128.
[15] M. Stern, A.L. Geary, J. Electrochem. Soc. 104 (1957) 56–61.
[16] L. Yijian, H. Jian, J. Mater. Sci. 26 (1991) 2833–2840.
[17] ASM Handbook: Alloy Phase Diagrams, vol. 3, ASM Intern., 1997.
[18] Y.P. Wu, P. Lin, C. Chu, Z. Wang, M. Cao, J. Hu, Mater. Lett. 61 (2007) 1867–1872.
[19] O. Maranho, D. Rodrigues, M. Boccalini Jr., A. Sinatora, Surf. Coat. Technol. 202 (2008) 3494–3500.
[20] H. Choi, S. Lee, B. Kim, H. Jo, C. Lee, J. Mater. Sci. 40 (2005) 6121–6126.
[21] D. Zois, A. Lekatou, M. Vardavoulias, I. Panagiotopoulos, A. Vazdirvanidis, J. Therm. Spray Technol. 17 (2008) 887–894.
[22] D. Shin, F. Gitzhofer, C. Moreau, J. Therm. Spray Technol. 16 (2007) 118–127.

[23] K.S. Narasimhan, F.J. Semel, in: Proceedings of the 2007 International Conference on Powder Metallurgy and Particulate Materials, May 13–16, Denver, Colorado, Metal Powder Industries Federation, Paper No. 2007-01-0145.
[24] V. Raghavan, J. Phase Equilib. Diffus. 28 (2007) 380–381.
[25] A. Inoue, B.L. Shen, C.T. Chang, Intermetallics 14 (2006) 936–944.
[26] Q. Wei, B. Yang, A. Jiang, Chin. Phys. Lett. 8 (1991) 296–299.
[27] H. Luo, D. Goberman, L. Shaw, M. Gell, Mater. Sci. Eng. A346 (2003) 237–245.
[28] M. Belkhaouda, L. Bazzi, A. Benlhachemi, R. Salghi, B. Hammouti, S. Kertit, Appl. Surf. Sci. 252 (2006) 7921–7925.